Reversible Vapochromic Luminescence Accompanied by Planar–Half-Chair Conformational Change of a Propeller-Shaped Boron β-Diketiminate Complex

Dr. Shunichiro Ito, Misao Yaegashi, Prof. Dr. Kazuo Tanaka* and Prof. Dr. Yoshiki Chujo

Department of Polymer Chemistry, Graduate School of Engineering, Kyoto University, Katsura, Nishikyo-ku, Kyoto 615-8510, Japan

E-mail: tanaka@poly.synchem.kyoto-u.ac.jp

Abstract: Leakage of volatile organic compounds (VOCs) is one of the most severe industrial accidents because it can cause environmental pollution, global warming, fire, and explosion. Hence the visualization of leakage is an essential technology to detect it at an early stage. Molecular crystals whose fluorescence color can be changed by the exposure to VOCs could potentially serve as the sensing materials for realizing rapid and facile VOC detection. These materials, however, usually require harsh conditions, such as heating or a vacuum, to recover their initial phases for reuse. Therefore, it remains a challenge to obtain completely reversible sensing systems without such energy-consuming recycling processes. Here we report the reversible color change of fluorescence from the crystals of a propeller-shaped boron β-diketiminate complex. The complex was crystallized in distinct crystalline phases having different luminescent colors. Importantly, these phases were interconverted very rapidly (time constant < 60 sec) and repeatedly upon exposure to the vapors of the appropriate VOCs. The small energy differences between conformers of the complex could lead to this pseudopolymorphic behavior. This finding could be applied for the development of further eco-friendly reversible sensing materials based on four-coordinated boron complexes.

Introduction

Sensing,[1–4] separation,[5–7] and storage[8–11] technologies of gaseous materials are of paramount importance for sustainable development. Porous materials (PMs) have been promising candidates for these usages because they absorb guest molecules into their voids derived from their long-ranged ordered structures and expel them by external stimuli like heating.[12–16] The physical properties of PMs depend drastically on the existence and absence, size, and electronic nature of guests. PMs which exhibit luminescent chromism in response to exposure to vapors of volatile organic compounds (VOCs), especially, are attractive materials for detecting a small amount of leakage of toxic or explosive gases and for security ink.[17–31] However, these compounds possess potential instability toward the air, moisture, and/or other harsh chemical conditions, and therefore a growing number of studies have recently reported chemically and physically stable PMs.[32,33]

Nonporous molecular crystals (NMCs), on the other hand, have no such functional voids in their packing patterns because of the absence of the polymeric or supramolecular structures derived from continuous valence, coordination, or hydrogen bonds. Nevertheless, various kinds of NMCs change their crystal structures by exposure to guest molecules. For instance, Lewis basic guests often increase the coordination numbers of transition metal complexes in NMCs, lead crystal–crystal transition, and alter the color, luminescence, or magnetic properties.[34–39] Although such specific affinities to guest compounds are useful for constructing stimuli-responsive systems, they often require harsh conditions to recover their initial states, for example, heating, drying in a vacuum, and both. Thus, the development of sensing materials towards VOCs without such affinities is still of importance for achieving stable and environment-friendly systems.

In this context, we show that conformational degrees of freedom are able to play a pivotal role in constructing stimuli-responsive NMCs. External stimuli can induce the interconversion between

some conformers when slight energy barriers separate them. As a result, the crystals of one of the conformers could transform into another one. For example, dimethoxy-substituted difluoroboron avobenzone exhibits polymorphs resulted from the existence of the syn–anti rotational conformers originating from the different mutual orientations of the two methoxy groups.[40] Some studies have reported similar conformational flexibility of other NMCs, *e.g.,* other difluoroboron avobenzones,[41,42] a platinum complex of 9-phenyl-9-arsafluorene,[43] and a gallium *β*-diketiminate complex.[44] However, there is a limited number of reports on completely reversible vapochromism of luminescent NMCs without the harsh conditions in their recycling process,[43] probably because tight crystal structures could hamper the flips between conformers.

The studies mentioned above suggest that the achievement of stimuli-responsive NMCs would need the following two characteristics. First, the conformers of a molecule should be separated by small potential energies to offer a possibility of (pseudo-)polymorphism. Second, the packing structures of NMCs should be relatively sparse so that the flips between the conformers would not be prohibited. Here, four-coordinated complexes of the group 13 elements possess the degree of freedom of out-of-plane bending of the boron atom from the central coordination ring (Figure 1a). [40,45] In addition to this degree of freedom, these complexes often exhibit luminescent chromism in response to external stimuli, such as mechanical grinding,[40,41,46–50] heating[51,52] and VOCs.[44] *β*-Diketiminate complexes would be advantageous concerning their efficient solid-state emission including aggregation- and crystallization-induced emission,[44,53–56] the designability of ligands, and chemical stability.[57–60] In this report, we hypothesized that such flexible and emissive *β*-diketiminate boron complexes might afford stimuli-responsive luminescent materials with low-energy recycling ability. A synthesized propeller-shaped boron complex showed aggregation- and crystallization-induced emission properties. Importantly, the complex crystallized into some

distinct phases depending on the solvents for crystallization: One phase contained only the complex, while the others were composed of the complex and solvent molecules. These pseudo-polymorphs exhibited different emission colors and repeatedly interconverted each other by treating with the vapor of VOCs at room temperature.

Results and Discussion

To realize a stimuli-responsive luminescent system consisted of boron β-diketiminates, we designed a propeller-like pentaphenyl boron complex (**PPB**, Figure 1b). The five phenyl groups were introduced into the central chelation ring because bulky substituents often induce sparse packing structures in the crystalline states.[61]

Single-point energy calculations of **PPB** in the gas phase were performed for some conformers with Gaussian 16 Rev. B package[62] at the M06/6-31+G(d,p) level of theory.[63] A potential energy surface of **PPB** along with the bent angle (θ) was calculated with partial optimizations, varying θ from 160º to 180º, and the other degrees of freedom were optimized (Figure 1c). The energy difference between the planar conformer ($\theta = 180°$) and the most stable half-chair conformation ($\theta = 172°$) is 0.59 kJ mol^{-1}. This value is significantly smaller than the rotational barrier of the methoxy group of anisole (13–19 kJ mol^{-1} in a solution)[64–66] or the ring-flip one of cyclohexane (43 kJ mol^{-1} in a solution).[67–69] Such a small value indicates that these conformers can be thermally accessible at room temperature.
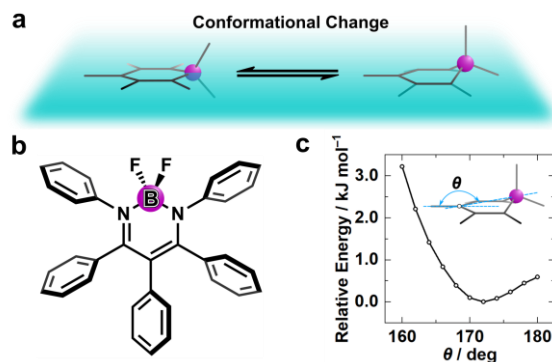
Figure 1. (a) Schematic illustration of the conformational change of boron complexes. The magenta sphere represents a boron atom. (b) A chemical structure of a *β*-diketiminate complex **PPB** investigated in this study. (c) Calculated potential energy surface along the bent angle *θ* depicted in the inset. The energy is relative to the value at *θ* = 172°.

Scheme 1 shows the synthetic method of **PPB**. The imine derivative **3** was prepared by condensation of aniline **1** and benzyl phenyl ketone **2**, according to the literature.[70] Deprotonation of **3** by *tert*-butyllithium, followed by the reaction with imidoyl chloride **4**, yielded a ligand **LH**. *tert*-Butyllithium gave the best result as a base for the preparation of the aza-enolate. Less bulky alkyllithium reagents, such as methyllithium, *n*- and *sec*-butyllithium, lead to nucleophilic addition to **3** as a side reaction. Lithium diisopropylamide, on the other hand, gave almost no product. The reaction between **LH** and trifluoroborane diethyl etherate in the presence of triethylamine afforded the complex **PPB**. The pure product was yielded by recrystallization from the mixed solution of hexane and ethyl acetate. The ^{11}B{^{1}H} spectrum exhibited a sharp triplet signal at 1.29 ppm, which is a distinctive feature of four-coordinated difluoroboron complexes.[54,55] The ^{13}C{^{1}H} spectra showed the characteristic peak assigned to the *α*-carbon of the *β*-diketimine moiety at 109.4 ppm.

Scheme 1. Synthetic scheme of a pentaphenyl boron *β*-diketiminate complex **PPB**
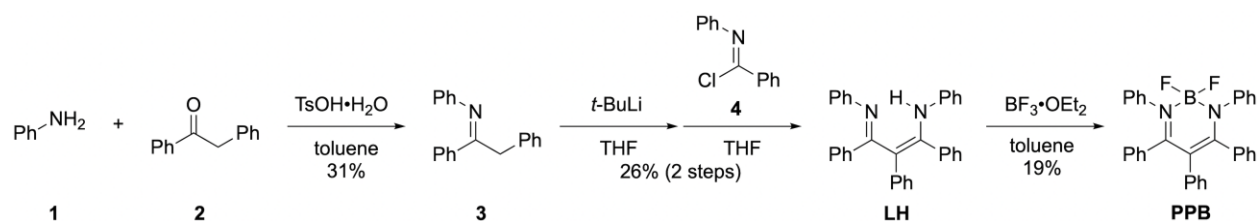
The absorption spectrum of **PPB** in the chloroform solution (1.0×10^{-5} M) is shown in Figure 2. The compound showed an absorption band at 370 nm (Table 1), which is comparable to the value of the tetraphenyl boron complex (376 nm).[54,55] This electronic transition should originate from the symmetrically allowed π–π* nature of the first singlet excited state S_1 of the compound.[56] This boron complex exhibited typical aggregation-induced emission (AIE) behavior (Figure 2). The absolute photoluminescence (PL) quantum yields of **PPB** in its dilute chloroform, THF and hexane/chloroform (99/1, vol/vol) solutions (1.0×10^{-5} M) were less than the limit of detection (< 0.01). The absorption and emission peaks of these dilute solutions were not dependent highly on the solvents. Figure 2 shows the emission spectra of the solution samples with different solvent compositions (1.0×10^{-5} M in mixed solvents of THF and water; the fraction of water = 1–99 %). The dependence of integrated emission intensity ratio A/A_0 on the fraction of water (f_w) is listed in Table 2, where A_0 is the integrated intensity at $f_w = 1$ vol%. The A/A_0 values significantly increased over 80 vol% of the water content, while the values in the low proportion of water were almost unity. The solutions containing over 80 vol% of water were turbid, and the absolute PL quantum yields (Φ_{PL}'s) of these water-rich suspensions were about 0.03. These results indicate that the formation of aggregates induces the emission enhancement of **PPB**. In the solution states, intra- and intermolecular motions and vibrations could non-radiatively consume the excitation energy at room temperature. These motions and vibrations, on the other hand, should be suppressed in the

aggregated states. Consequently, this complex is allowed to emit stronger in the aggregated state than in the solution state.[54–56] Notably, the A/A_0 decreased at the 99 vol% of the water content, but still higher than those under the conditions with a low concentration of water (< 80 vol%). This decrease may originate from the precipitation of the large aggregates.
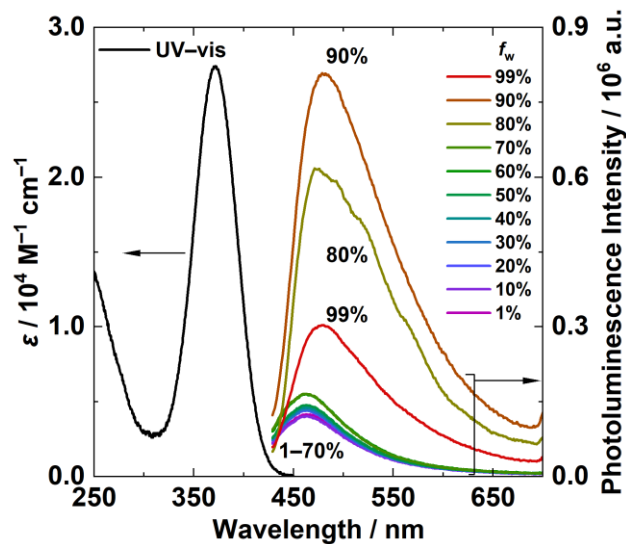

Figure 2. An absorption spectrum of **PPB** in chloroform solution (1.0×10^{-5} M, black solid) and photoluminescence spectra of **PPB** in mixed solvents of THF and water (1.0×10^{-5} M, colored solid) with different water contents ($f_w = 1$–99 vol%).

Manuscript for Chemistry—A European Journal

Table 1. Photophysical properties of **PPB** in solution states[a]

Solvent	Condition	λ_{abs} / nm	ε_{max} / 10^4 M^{-1} cm^{-1}	λ_{FL} / nm	Φ_{PL}
CHCl$_3$	r.t.	370	2.74	464	< 0.01
THF	r.t.	371	3.05	465	< 0.01
hexane/CHCl$_3$ (99/1, vol/vol)	r.t.	374	3.37	463	< 0.01
2-MeTHF	r.t.	372	3.34	463	< 0.01
	77 K	n.d.[b]	n.d. [b]	432	1.0

[a] In dilute solutions (1.0 × 10^{-5} M) at r.t. and 77 K. [b] Not determined.

Table 2. Dependency of emission properties towards the fraction of water

f_w (%)[a]	1	10	20	30	40	50	60	70	80	90	99
λ_{em} / nm	467	464	464	464	462	463	463	462	471	479	480
A/A_0[b]	1	0.95	1.03	1.05	1.09	1.12	1.28	1.28	6.28	8.42	2.98
Φ_{PL}[c]				< 0.01					0.04	0.04	0.03

[a] Volume fraction of water of mixed solvents of THF/water. [b] Integrated intensity (A) of photoluminescence normalized to the integrated intensity at f_w = 1% (A_0). [c] Absolute photoluminescence quantum yield.

The electronic nature in the excited state of a single molecule of the complex was investigated with photophysical measurements for a dilute 2-methyltetrahydrofuran (2-MeTHF) solution (1.0 × 10^{-5} M) at room temperature and 77 K. The absorption band (λ_{max} = 372 nm) was almost identical to those in the other solvents. The solution was not emissive at room temperature (Φ_{PL} < 0.01) as well as in the other solvents but was emissive at 77 K (λ_{PL} = 432 nm, Φ_{PL} = 1.0; Table 1). The long-lifetime phosphorescence spectrum was detected at 521 nm (τ_{Phos} = 0.64 sec) when the spectrum was recorded 1.0 msec after the excitation in order to eliminate background fluorescence

interference. The intensity of the phosphorescence, however, was too weak to be distinguished from the fluorescence in the steady-state spectrum. Consequently, the quenching of the S_1 state through intersystem crossing from the singlet state to triplet states should be a minor process.

Distinct crystal phases were obtained by changing solvents for recrystallization. The yellow crystals obtained from hexane/EtOAc exhibited weak green emission (Phase G) at room temperature under UV irradiation (365 nm), while the colorless crystals obtained from hexane/dichloromethane (DCM) showed intense blue emission (Phase B, Figure 3a). Powder X-ray diffraction (PXRD) profiles were different from each other (Figure 3b). ^{1}H NMR spectrum of Phase B showed the peak at 5.30 ppm assigned to DCM, meanwhile that of Phase G was identical to that of the pure **PPB** powder. The integration ratio of the peak of DCM against the peaks of **PPB** in the ^{1}H NMR signals indicates that Phase B contains the complex and DCM in the molar ratio of 1:1. In addition, a profile of the thermogravimetric analysis of Phase B showed 11.4% of weight loss at 67.3 °C (Figure 3c). This experimental value is in good agreement with the estimated value for the dissociation of DCM from the 1:1 mixture of **PPB** and DCM (14.6%). Consequently, it was revealed that **PPB** exhibits pseudopolymorphism.
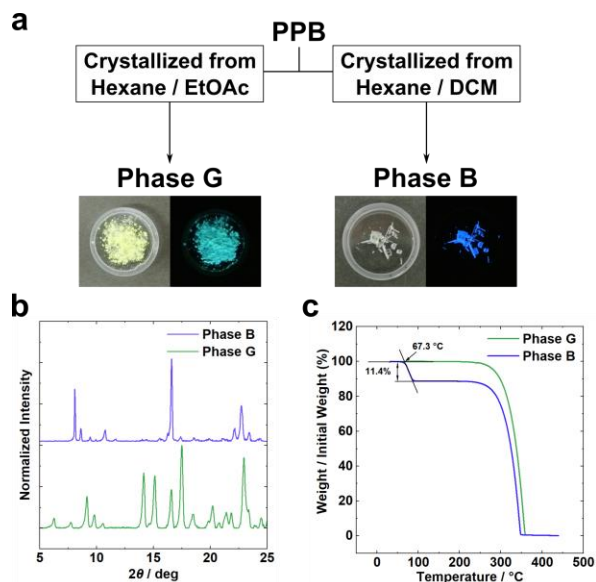
Figure 3. (a) Preparation methods of Phases G and B. Pictures of Phases G and B were taken under natural light (left panels) and UV irradiation (right panels). (b) Powder X-ray diffraction patterns for Phases G and B. (c) Thermogravimetric analysis profiles for Phases G and B.

A crop of crystals of Phase B was grown from a hexane/DCM solution and suitable for a single-crystal X-ray diffraction (SCXRD) analysis. Conversely, Phase G appeared only as a crystalline powder when the compound was recrystallized from hexane or hexane/EtOAc solutions. Therefore, the PXRD data of Phases G and B were analyzed, and subsequently their crystal structures were refined by using the Rietveld method (Figure 4). Both phases belong to the monoclinic space group $P2_1/n$ (No. 14). The asymmetric units of Phases G and B contain one **PPB** molecule, and one **PPB** and one DCM molecules, respectively. Importantly, the complex in Phase G shows a half-chair conformation ($\theta \sim 165°$), while the structure in Phase B is a planar conformation ($\theta \sim 180°$). As shown in Figure 1, the relative energies of the optimized structures with fixed bent angles 165° and 180° are *ca.* 0.9 and 0.6 kJ mol^{-1}, respectively. Hence these conformers would be thermally redistributable at room temperature when there is no external potential.
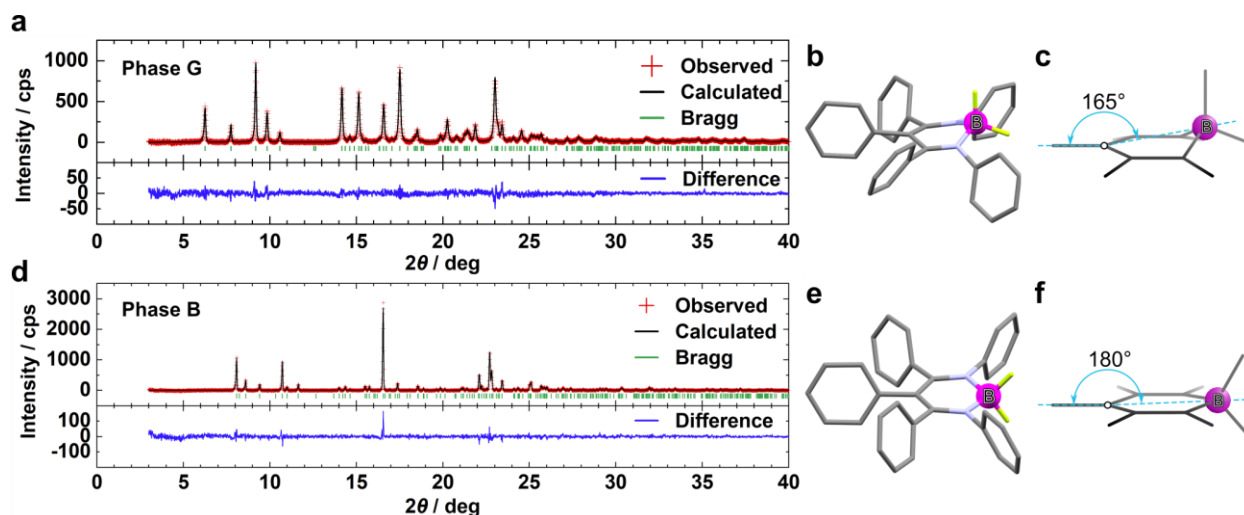
Figure 4. Rietveld plots for (a) Phase G and (d) Phase B. Red crosses, green tics, black line, and blue line represent the observed data, the positions of Bragg reflections, the calculated data, and the differences between the observed and calculated data. A single molecular structure (b, e) and the bent angles (c, f) for Phase G and Phase B, respectively.

To elucidate the electronic nature of the complex in Phases G and B, diffuse reflectance and PL spectra were recorded (Figure 5). Both diffuse reflectance spectra of Phases G and B show an electronic transition band at 367 nm (3.38 eV), which is comparable to that of the dilute solution (370 nm; Table 4). An additional transition band was observed at around 440 nm (2.82 eV) only in the spectrum of Phase G. This sideband is responsible for the yellow color of the powder of Phase G. This fact indicates that the lower electronic state is formed in Phase G. The PL spectrum of Phase G was also detected in the lower energy region (490 nm) than that of Phase B (443 nm). According to Kasha's rule, the red-shifted emission band should be attributed from the additional band which appears in Phase G. Indeed, the fluorescence at 490 nm was observed when the sample of Phase G was excited at 440 nm as well at 367 nm.

Table 4. Photophysical properties of Phases G and B[a]

Phase	λ_{ref} / nm	λ_{FL} / nm	Φ_{PL}
Phase G	367, 440	490	0.03
Phase B	367	443	0.66

[a] Photoluminescence spectra were recorded under excitation at 370 nm.
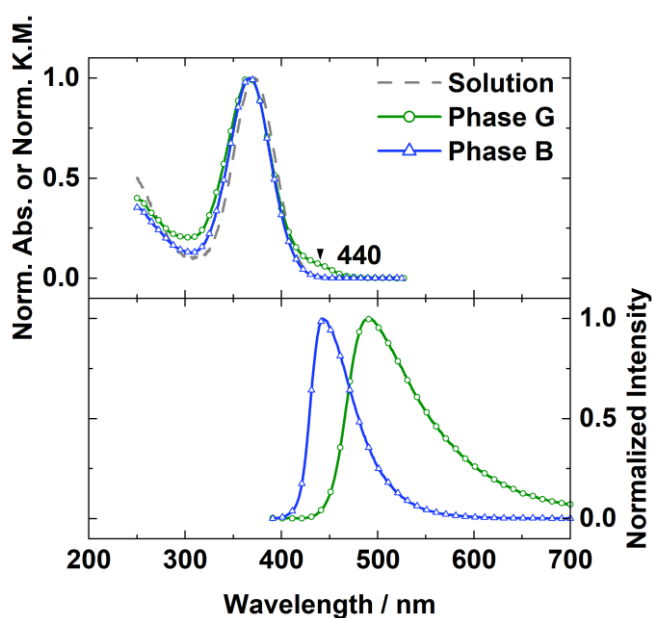

Figure 5. Normalized diffuse reflectance (upper panel) and normalized photoluminescence (lower panel) spectra of Phases G and B. Diffuse reflectance spectra were converted with a Kubelka–Munk (KM.) function. Gray dashed line shows an absorption spectrum of **PPB** in a chloroform solution (1.0 × 10⁻⁵ M).

To obtain further insight into the electronic properties of **PPB**, a series of density functional theory (DFT) and time-dependent DFT (TD-DFT) calculations were carried out. The levels of

theory were the (TD-)M06/6-31+G(d,p) and (TD-)M06/6-311++G(d,p) for geometry optimizations and single-point energy calculations, respectively. The optimized structure of the complex in a vacuum at the S_0 state for a single molecule shows a half-chair conformation ($\theta = 171.96°$). As shown in Table 5, the transition energy corresponding to the S_0–S_1 electronic transition was estimated to be 3.48 eV (357 nm), which is comparable to the experimental value of the absorption maximum 3.35 eV ($\lambda_{abs} = 370$ nm). Highest occupied (HO) and lowest unoccupied (LU) molecular orbitals (MOs) for the optimized geometry are shown in Figure 6. The S_1 state was assigned to the symmetrically allowed HOMO–LUMO transition, which has π–π* nature.[56]

The effects of the bent angle θ on the properties of the electronic transition of a single molecule were evaluated. The parameters for the corresponding electronic transitions were calculated by using the optimized structures with the fixed θ (= 160° and 180°), as shown in Table 5. The transition energies varied in the small range of 3.44–3.54 eV (361–351 nm). These results indicate that the low-energy absorption band observed in Phase G ($\theta = 165.11°$) would not be reproducible in a regime of a single molecule.

Table 5. Calculated parameters of the S_0–S_1 electronic transitions for single molecules with some geometries

θ / deg[a]	Energy / eV[b]	λ / nm	f[c]	Composition	Coefficient[d]
160	3.44	361	0.4150	HOMO $\rightarrow$ LUMO	0.70326
172[e]	3.48	357	0.4181	HOMO $\rightarrow$ LUMO	0.70312
180	3.54	351	0.4145	HOMO $\rightarrow$ LUMO	0.70280

[a] Bent angle. [b] Transition energy. [c] Oscillator strength. [d] Expansion coefficient for the electronic transitions. [e] An optimized geometry in the singlet ground state.
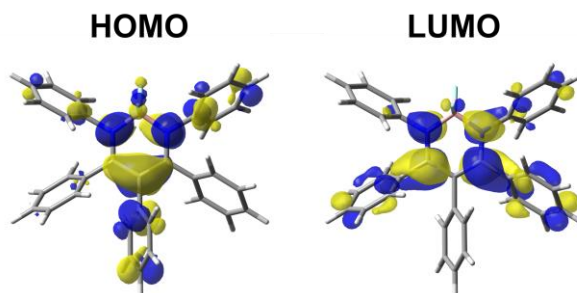
Figure 6. HOMO and LUMO distributions of the optimized structure of **PPB**.

Next, we calculate transition energies considering intermolecular interactions between the nearest neighbor dimers (NNDs) in the crystal structures of Phases G and B in order to elucidate the origin of the lower energy absorption band. Typical intermolecular interactions that lead to the large energy change of electronic transitions are H- and J-type excitonic couplings and intermolecular charge transfer.[71,72] For a system composed of a dimer, the excitonic couplings are expressed as the interactions between the electronic transition dipole moments (μ_{el}) of the two molecules (Figure 7a). When the two dipoles couple each other, two delocalized excited states are generated. The strength of the coupling is evaluated with a value of Coulomb coupling J_C:

$$J_C = \frac{\mu_{el}^2(1 - 3\cos^2\phi)}{4\pi\varepsilon R^3}, \tag{1}$$

where φ is the angle formed by the two dipoles ($0° < \varphi < 90°$), ε is the dielectric constant, and R is the distance between the dipoles. The two states split by $2|J_C|$ consist of allowed "in-phase" and forbidden "out-of-phase" states. H-aggregates maintain a "side-by-side" orientation where φ is larger than the so-called "magic angle" $\varphi_M = 54.7°$. In this case, a Coulomb coupling is positive ($J_C > 0$). Conversely, J-aggregates maintains a "head-to-tail" orientation ($0° < \varphi < \varphi_M$) leading to a negative Coulomb coupling ($J_C < 0$). In Phases G and B, the angles φ between the two dipoles of the NNDs (Figures 7b and 7c) are 78.4° and 56.3°, respectively. Therefore, both of these dimers constitute H-aggregates where the lower-energy state is an optically dark "out-of-phase" state. The coupling strengths were estimated by using TD-DFT calculations at the M06/6-311++G(d,p) level of theory. The values corresponding to $2|J_C|$ of Phases G and B are 0.07 and 0.04 eV, respectively (Figures 7f and 7g, Table 6). These values were considerably small compared to the energy difference between main and sidebands in the diffuse reflectance spectrum of Phase G (0.56 eV). It is worth to note that such small interactions should originate from the large intermolecular distances (Phase G: 6.49 Å; Phase B: 6.59 Å) likely due to the steric hindrance of the peripheral aromatic rings. These results indicate that excitonic couplings between molecules separated by longer distances than the NNDs should be much smaller. Consequently, the excitonic couplings would play a limited role in the formation of the sideband.
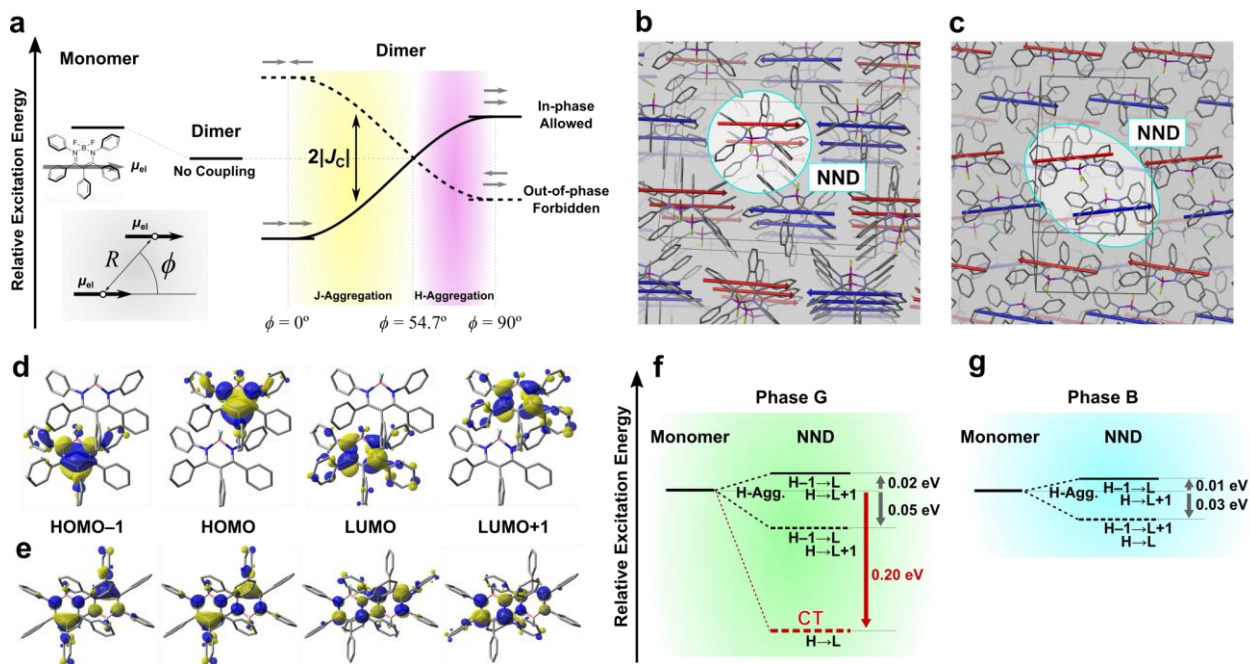
Figure 7. (a) Schematic representation of excitonic coupling. (b, c) Packing structures of Phases (b) G and (c) B. Red and blue vectors represent electronic-transition dipole moments of each molecule. Cyan circles highlight nearest neighbor dimers (NNDs) for theoretical calculations. (d, e) Molecular orbital distributions of the NNDs for Phases (d) G and (e) B. (f, g) Relative transition energies obtained by considering intermolecular interactions between the NNDs for Phases (f) G and (g) B. H and L denote HOMO and LUMO, respectively.

TD-DFT calculations for the NND in Phase G, on the other hand, revealed that the intermolecular CT could form a low-energy state. The HOMO localized at a single molecule, whereas the LUMO localized at the other (Figure 7d). The lowest excited state of the NND is composed of the HOMO–LUMO transition, indicating that an electron on a complex would transfer into the other one during a photoexcitation. This CT state was located 0.20 eV below the S_1 state of the monomer having the geometry in Phase G (Figure 7f, Table 6). The corresponding oscillator strength of the CT state was estimated to be 0.0003, meaning that the strength of the

electronic transition attributed to this CT state should be quite low. Such a CT state was not produced in the packing structures of Phase B (Figures 7e and 7g, Table 6). Hence, the sideband observed in the diffuse reflectance spectrum of Phase G could be assigned to the transition to the intermolecular CT state. The interactions of three or more molecules could result in the lower energy state (440 nm; 2.82 eV) observed in the absorption spectrum of Phase G. According to Kasha's rule, the low PL quantum yield of Phase G is also derived from the small oscillator strength of the CT state. The slight energy difference (40 meV) between the dimeric states in Phase B could allow excitons to be activated thermally from the dark out-of-phase state to the emissive in-phase state. It should be mentioned that the results of the calculations for Phase B were hardly affected when a DCM molecule included in Phase B was considered.

Table 6. Results of DFT calculations for single molecules and NNDs in Phases G and B

Phase	Structure	State	E / eV[a]	λ / nm	f[b]	Composition [c]	Coeff. [d]
G	Monomer	S_1	3.55	349	0.4007	H → L	0.70254
	NND	S_1 (CT)	3.35	370	0.0003	H → L	0.70539
		S_2 (out-of-phase)	3.50	354	0.0013	H–1 → L	0.46898
						H → L+1	0.51906
		S_3 (in-phase)	3.57	347	0.6707	H–1 → L	0.51759
						H → L+1	–0.47229
B	Monomer	S_1	3.77	329	0.4177	H → L	0.70198
	NND	S_1	3.74	331	0.0006	H–1 → L+1	0.46502
						H → L	0.49149
		S_2	3.78	328	0.7157	H–1 → L	0.48128
						H → L+1	0.49124

[a] Transition energy. [b] Oscillator strength. [c] Composition of the electronic states. H and L denote HOMO and LUMO, respectively. [d] Expansion coefficient for the electronic transition.

Remarkably, Phases G and B can repeatedly interconvert by fuming the vapor of DCM or hexane. The crystalline powder of Phase G was transformed into Phase B upon exposure to DCM vapor for 15 h at room temperature. The powder of Phase B, on the other hand, was converted to Phase G spontaneously but very slowly without the DCM vapor. (Phase B remained after a year.) This phase transition from Phase B to Phase G was accelerated upon exposure to the hexane vapor. This means that Phase B is a stable phase only under the DCM vapor, and is a metastable without it. The hexane vapor can accelerate this spontaneous process probably because the hexane molecules

could enhance the molecular mobility of **PPB** and DCM molecules on the surface of the crystals of Phase B.

The dynamics of the phase transitions between Phase B and Phase G were evaluated by recording the PL spectra of the samples at different treatment time (Figure S3). The time constant of the transition from Phase G to Phase B was estimated to be 28 sec. On the other hand, the kinetics of the transition from Phase B to Phase G involve two distinct time constants, 53 sec and 4 hours. The fast component in each transition may be attributed to the solvation–recrystallization process. These very rapid transitions between the two phases enable us to detect the VOC gases in real time. The slow component in the transition from Phase B to Phase G might be originated from the permeation process of hexane molecules into the intact parts buried in the outer layer in which the B-to-G phase transition has been accomplished. This deacceleration effect may like the passivation of metals. The time constant of this slow component seemed to depend strongly on the particle size of the powder. In addition, it is worth to note that **PPB** was deliquescent with DCM but not with hexane. This might mean that the solvation of the surface molecules by DCM is much more favorable than by hexane. Therefore, thin layer of the concentrated solution of **PPB** could be formed on the surfaces of the crystals under the DCM vapor. Such a solvated layer could accelerate the phase transition.

The reversibility of this interconversion was monitored with PL spectroscopy and PXRD (Figure 8). The PL maxima and the PXRD patterns were identical to those of the corresponding phases in each cycle. Typical nonporous molecular crystals (NMCs) need to dry in a vacuum or upon heating or immerse to the liquids of solvents in order to recycle the materials.[43] In contrast, the **PPB** crystals can be recycled only using the vapors of VOCs under ambient condition. It should be mentioned that the weak emission band was observed in the shorter wavelength region (400–450

nm) after the treatments with hexane even for 48 h. This result indicates that the small amount of

Phase B would remain in the hexane-fumed sample. Because of the deliquescence of **PPB** with

DCM, sometimes the size of the crystals of **PPB** changes during the G-to-B transitions. Hence, the

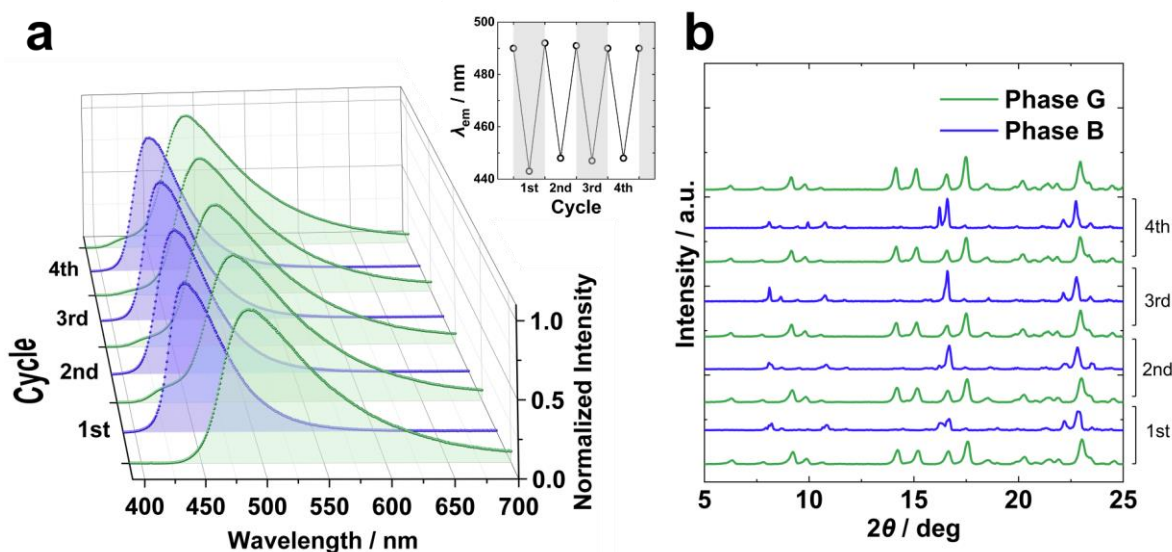fractions of the remaining Phase B were not identical between the cycles.

Figure 8. (a) Photoluminescence spectra of Phases G (green) and B (blue) in each cycle.
Crystalline samples were excited at the absorption maxima of a chloroform solution (λ_{abs} = 370
nm). Inset represents the wavelengths at the luminescence maxima (λ_{max}) for each cycle. (b)
Powder X-ray diffraction profiles for each cycle.

To investigate effects of the kind of VOCs on the vapochromic behavior, we treated the crystals

of Phase G with the vapor of 16 kinds of VOCs for 15 h. As shown in Figure 9, the relatively small

and aprotic six kinds of VOCs (Group I) induced the luminescence-color change from green to

blue, the other ten kinds of VOCs induce no change (Group II). PL spectra of the crystals, including

the group I VOCs except for DMF, were observed at around 440–465 nm (Figure 9b). These

maximum PL wavelengths were slightly different, probably due to the differences of polarity and movability of the molecules in the phases, or maybe due to different packing structures. For the phase exposed to the DMF vapor, the PL spectra showed a maximum peak at 500 nm and a shoulder peak at around 430 nm. This result means that the phase transition induced by the DMF vapor should be not completed under this condition. Indeed, after the exposure of the DMF vapor for three days at room temperature, the peak at 500 nm disappeared completely, and a peak at 434 nm was observed. The ^{1}H NMR spectra of the blue-emissive crystal phases showed the peaks attributed to those of the corresponding VOCs in group I. The molecular ratios between the complex and the VOCs were calculated to be 1:1 by using the integration ratios of the ^{1}H NMR signals. The blue-emissive phases prepared with the Group I VOCs exhibited completely different PXRD patterns compared to Phase G (Figure 9c). Therefore, these group I VOCs cause the crystal–crystal transitions from Phase G to the blue-emissive phases composed of **PPB** and the VOC molecules in the 1:1 molar ratio, like DCM. The original packing of Phase G, which would lead to the green-emissive CT state, might be eliminated by the guest solvent molecules. Surprisingly, the vapor of DMSO induced the phase transition, although DMSO has a quite low vapor pressure (0.08 kPa). Thus, high vapor pressures of VOCs were not necessary for the induction of the phase transition.

In contrast with Group I, the ten VOCs in Group II lead to phase transitions from the blue-emissive phases to Phase G (Figure 9d). PXRD and ^{1}H NMR revealed that Phase G was recovered from all blue-emissive phases containing Group I VOCs after exposure of Group II VOCs for 15 h. The PL peaks attributed to the blue-emissive phases were suppressed entirely, and the characteristic peak of Phase G was observed from all the samples fumed by Group II VOCs. ^{1}H NMR spectra and PXRD profiles of the powders were absolutely identical to those of Phase G,

indicating that Group II molecules accelerate the exclusion of the guest molecules from the crystalline phase containing the Group I VOCs.

There might be two key factors distinguishing Group I and Group II: solubility of **PPB** and size/shape of the solvent molecules. All the molecules in Group I are good solvents for **PPB**. On the other hand, hexane, pentane, methanol, ethanol, diethyl ether, and cyclohexane are not. The molecules of poor solvents could not effectively solvate the **PPB** molecules and might not be able to stabilize crystalline states involving the solvent molecules. Even if the solvents are good solvents for **PPB** (ethyl acetate, THF, chlorobenzene, and toluene), stable crystalline phases could not be formed because of the mismatch between the size/shape of the solvent molecules and the structural features of the solvent sites in available crystal packing structures of **PPB**.[44]
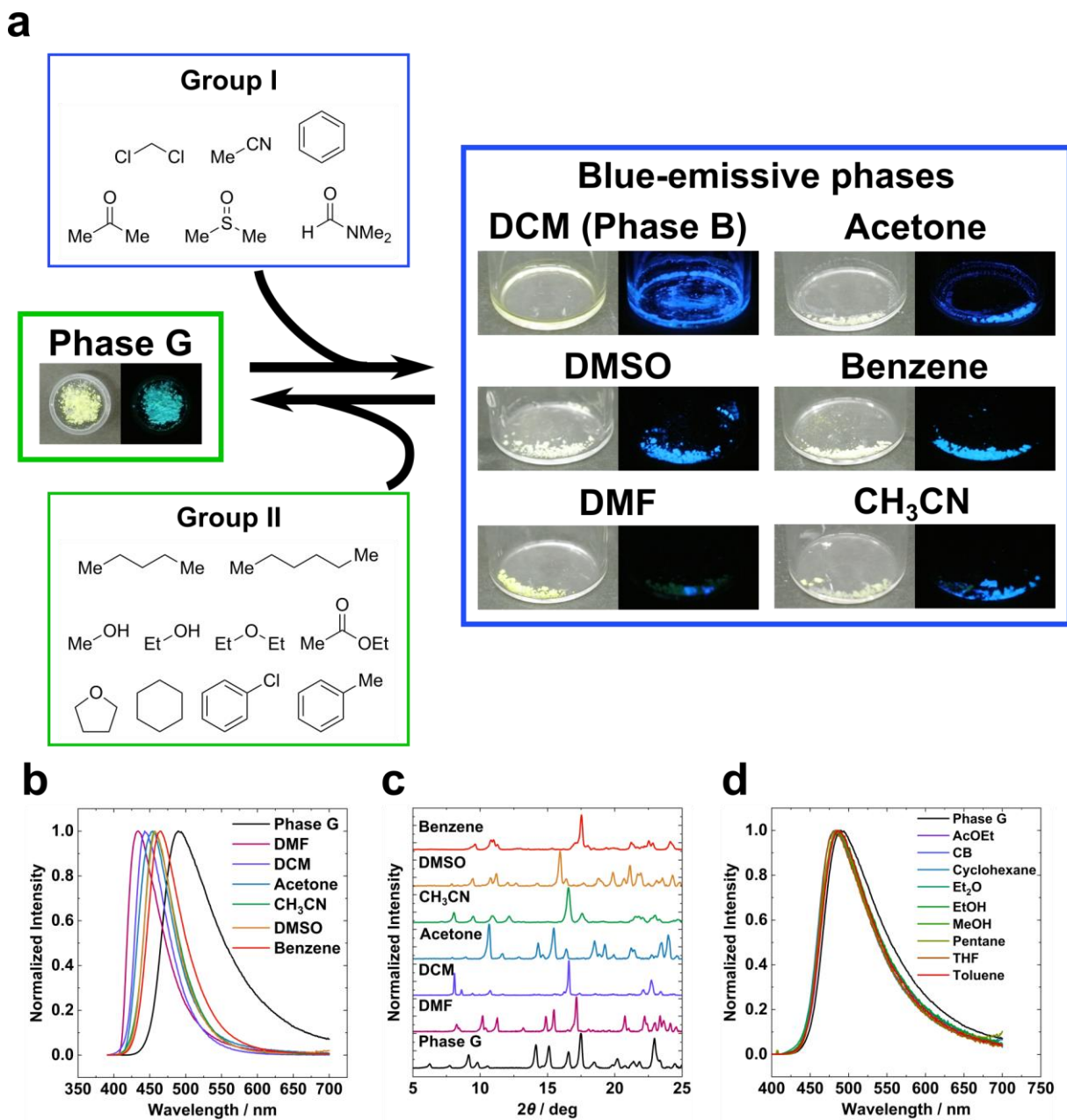
Figure 9. (a) Reversible vapochromic behavior of **PPB**. (b) Photoluminescence spectra of blue-emissive phases including the group I molecules. A solid black line shows a photoluminescence spectrum of Phase G. (c) Powder X-ray diffraction profiles of the blue-emissive phases and Phase G (solid black line). (d) Photoluminescence spectra of the powders recovered by the group II compounds from Phase B.

Experimental Section

Characterization Methods: ^{1}H (400 MHz) and ^{13}C{^{1}H} (100 MHz) NMR spectra were recorded on the JEOL JNM-AL400 spectrometer. In ^{1}H and ^{13}C{^{1}H} NMR spectra, tetramethylsilane (TMS) and/or residual solvent peaks was used as an internal standard. High-resolution mass (HRMS) spectrometry was performed at the Technical Support Office (Department of Synthetic Chemistry and Biological Chemistry, Graduate School of Engineering, Kyoto University), and the HRMS spectra were obtained on a Thermo Fisher Scientific EXACTIVE spectrometer for electrospray ionization (ESI). Elemental analysis was performed at the Microanalytical Center of Kyoto University.

Materials: All reactions were performed under argon atmosphere using modified Schlenk line techniques unless otherwise noted. Analytical thin-layer chromatography (TLC) was performed with silica gel 60 Merck F254 plates. Column chromatography was performed with Wakogel C-200 SiO_2. All chemicals were purchased from commercial sources (FUJIFILM Wako Pure Chemical Corporation, Tokyo Chemical Industry Co., Ltd., Sigma-Aldrich Co. LLC. or Kanto Chemical Co., Inc.) and used as received. Tetrahydrofuran (THF), diethyl ether (Et$_2$O), and triethylamine (Et$_3$N) were purified using a two-column solid-state purification system (Glass Contour Solvent System, Joerg Meyer, Irvine, CA). Compounds **3**[70] and **4**[54] were synthesized according to the previous reports.

Synthesis of LH: To a solution of **3** (0.2 g, 0.74 mmol, 1 equiv.) in THF (6 mL) was added *tert*-butyllithium (0.8 mL, 1.22 mmol, 1.52 M in *n*-pentane, 1.6 equiv.) dropwise at –78 °C over 1 h. The reaction mixture was stirred at –78 °C for 0.5 h, and then **6** (0.50 g, 2.3 mmol) in THF (6 mL) was added to the mixture at –78 °C. After stirred the solution at –78 °C for 1.5 h, and then at ambient temperature for 18 h under an argon atmosphere, the solution was quenched with saturated

aqueous NH_4Cl and stirred at 0 °C. The solution was washed with brine and dried over anhydrous sodium sulfate. After the solvent was removed by a rotary evaporator, the product was purified by silica gel column chromatography two times with hexane/ethyl acetate = 9/1 as an eluent (R_f = 0.33). The obtained product was dried in vacuum to give crude **LH** as a yellow solid (90 mg, 26 %). The crude product was used as such without further purification. ^{1}H NMR (400 MHz; CDCl$_3$) δ = 7.92–7.90 (m, 2H, *Ar*), 7.4–6.4 (m, 23H *Ar*), 6.00 (s, 1H, N*H*) ppm. HRMS (ESI) for [M+H]$^+$: Calcd., 451.2169; found, 451.2163.

Synthesis of PPB: To a solution of crude **LH** (0.086 g, 0.19mmol, 1 equiv.) in toluene (2.5 mL) was added BF$_3$·OEt$_2$ (0.42 mL, 0.48 g, 3.42 mmol) at ambient temperature. After the solution was stirred at 50 °C for 23 h under an argon atmosphere, the reaction was stopped by cooled to ambient temperature. The reaction mixture was washed with water and brine and then dried over anhydrous sodium sulfate. After the solvent was removed by a rotary evaporator, the product was purified by silica gel column chromatography (eluted with hexane/ethyl acetate = 9/1, R_f = 0.14). The obtained product was recrystallized from a mixed solvent of hexane/ethyl acetate (5/1). The precipitate collected by filtration was dried in vacuum to give pure **PPB** as a yellow crystal (0.018 g, 19%). ^{1}H NMR (400 MHz; CDCl$_3$) δ = 7.19 (d, *J* = 7.7 Hz, 4H), 7.12 (t, *J* = 7.7 Hz, 4H), 7.04 (t, *J* = 7.2 Hz, 2H), 6.91 (m, 10H), 6.77 (m, 3H), 6.71 (m, 2H). ^{13}C{^{1}H} NMR (101 MHz; CD$_2$Cl$_2$) δ = 165.8 (*C*=N), 141.9, 137.5, 135.6, 133.4, 129.7, 128.6, 128.1, 127.8, 127.2, 127.1, 126.5, 125.6, 109.4 (N=C–*C*=C–N) ppm. ^{11}B{^{1}H} NMR (128.4 MHz; CDCl$_3$) δ = 1.29 (t, ^2J = 31.2 Hz) ppm. HRMS (ESI) for [M+H]$^+$: Calcd., 521.1971; found, 521.1965.

Photophysical Measurements: UV−vis absorption spectra were recorded on a SHIMADZU UV–3600 spectrophotometer. Fluorescence and phosphorescence emission spectra and phosphorescence decay were measured with a HORIBA JOBIN YVON Fluorolog-3

spectrofluorometer. Absolute photoluminescence quantum yields were measured with a Hamamatsu Photonics Quantaurus-QY Plus C13534-01. Photoluminescence (PL) lifetimes were measured by a Horiba FluoroCube spectrofluorometer system with an Oxford Optistat DN for temperature control and a UV diode laser (NanoLED 375 nm).

Single-Crystal X-ray Diffraction: Data were collected using a Rigaku R-AXIS RAPID-F with graphite-monochromated Mo Kα radiation diffractometer and an imaging plate. Data were collected at 93 K. Equivalent reflections were merged, and a symmetry-related absorption correction was carried out with the program ABSCOR.[73] The structures were solved with SHELXT 2014[74] and refined on F^2 with SHELXL[75] on Yadokari-XG[76] or ShelXle.[77] The program ORTEP-3[78] was used to generate the X-ray structural diagram.

Powder X-Ray Diffraction Analysis: The analyzed PXRD data were measured using Rigaku SmartLab with a Ge (111) Johannson monochromator (Cu Kα_1 radiation λ = 1.54059 Å, 40 kV and 30 mA, transmittance mode), a D/tex Ultra detector, and a capillary rotation attachment. The analyses were carried out with the powder X-ray diffraction analysis software PDXL2. For all the compounds, indexing programs DICVOL[79] or ITO[80] were used for the determination of cell dimensions. The diffraction profiles were decomposed with the whole powder pattern fitting (WPPF) method. Following these data, corresponding space groups were determined based on systematic extinctions. After additional WPPF methods, the initial phases of Phases G and B were obtained by direct space method using the DFT-optimized structures of **PPB** at the M06/6-311++G(d,p) level of theory. These obtained structures were refined using the Rietveld method under restrained conditions for bond lengths and angles obtained from the Cambridge Structural Database System (CSDS) via Mogul Server Ver. 1.0. Restraint stiffness, s_{res} (defined by Eq. (4)), was determined as σ_{Norm} (defined by Eq. (8)) becomes a proximate value to one. We determined

converged structure, confirming residual sum of squares, R_{wp}, was less than 10%, and goodness-of-fit indicator, S, sufficiently closed to unity.

Fitting parameters for the Rietveld refinement were defined as follows:

$$R_p = \frac{\sum_i |y_i - y_i^{cal}(p)|}{\sum_i |y_i|} \tag{1}$$

$$R_{wp} = \sqrt{\frac{\sum_i w_i \left(y_i - y_i^{cal}(p)\right)^2}{\sum_i w_i y_i^2}} \tag{2}$$

$$R_e = \sqrt{\frac{N - p}{\sum_i w_i y_i^2}} \tag{3}$$

$$S = \frac{R_{wp}}{R_e} \tag{4}$$

$$R = R_{wp} + s_{res}(R_{res}^d + R_{res}^a) \tag{5}$$

$$R_{res}^d = \sum_i^{M_d} \left(\frac{d_{0i} - d_i}{\sigma_i^d}\right)^2 \tag{6}$$

$$R_{res}^a = \sum_j^{N_a} \left(\frac{a_{0i} - a_i}{\sigma_i^a}\right)^2 \tag{7}$$

$$\sigma_{Norm} = \sqrt{\frac{R_{res}^d + R_{res}^a}{M + N}}, \tag{8}$$

where y_i is a diffraction intensity, $y_i^{cal}(p)$ is a calculated intensity, p is a parameter for the least-squares method, w_i is a weight, N is the number of data points, M_d is the number of restraints for bond length, and N_a is the number of restraints for bond angles. In addition, d_{0i} and a_{0j} are mean bond lengths and angles of similar structures, respectively. σ_i^d and σ_j^a are standard deviations of mean bond lengths and angles, respectively.

Conclusions

The propeller-like pentaphenyl boron *β*-diketiminate complex **PPB** was synthesized. **PPB** exhibited pseudopolymorphism probably because of the conformational degrees of freedom between a planar conformation and a half-chair conformation. The emission color of the pure **PPB** crystal (Phase G) is green, meanwhile that of the crystals containing DCM molecules (Phase B) is blue. The low-energy photoluminescence of Phase G could originate from the intermolecular CT state. Furthermore, the crystals of Phase G were transformed into the blue-emissive crystalline phases by the treatments with the vapors of the relatively small and aprotic six kinds of VOCs. The VOCs which were not constructed co-crystals with **PPB** induced the phase transition from the blue-emissive crystals to Phase G. This novel complex with reversibly vapochromic luminescence can be utilized for advanced stimuli-responsive electronic materials such as rewritable memories and recyclable sensors.

Acknowledgements

Supporting Information description

Deposition numbers^^<url href="https://www.ccdc.cam.ac.uk/services/structures?id=doi:10.1002/chem.20210XXX">2061741 (for **PPB·DCM**) and 2062123 (for Phase B of **PPB**) and 2062124 (for Phase G of **PPB**)</url> contain the supplementary crystallographic data for this paper. These data are provided free of charge by the joint Cambridge Crystallographic Data Centre and Fachinformationszentrum Karlsruhe <url href=" http://www.ccdc.cam.ac.uk/structures ">Access Structures service</url>

References

[1] R. A. Potyrailo, C. Surman, N. Nagraj, A. Burns, *Chem. Rev.* **2011**, *111*, 7315–7354.

[2] X. Zhou, S. Lee, Z. Xu, J. Yoon, *Chem. Rev.* **2015**, *115*, 7944–8000.

[3] R. A. Potyrailo, *Chem. Rev.* **2016**, *116*, 11877–11923.

[4] Z. Li, J. R. Askim, K. S. Suslick, *Chem. Rev.* **2018**, *119*, 231–292.

[5] N. W. Ockwig, T. M. Nenoff, *Chem. Rev.* **2007**, *107*, 4078–4110.

[6] S. Das, P. Heasman, T. Ben, S. Qiu, *Chem. Rev.* **2016**, *117*, 1515–1563.

[7] Q. Qian, P. A. Asinger, M. J. Lee, G. Han, K. M. Rodriguez, S. Lin, F. M. Benedetti, A. X. Wu, W. S. Chi, Z. P. Smith, *Chem. Rev.* **2020**, *120*, 8161–8266.

[8] M. P. Suh, H. J. Park, T. K. Prasad, D.-W. Lim, *Chem. Rev.* **2012**, *112*, 782–835.

[9] K. V. Kumar, K. Preuss, M.-M. Titirici, F. Rodríguez-Reinoso, *Chem. Rev.* **2017**, *117*, 1796–1825.

[10] K. Sordakis, C. Tang, L. K. Vogt, H. Junge, P. J. Dyson, M. Beller, G. Laurenczy, *Chem. Rev.* **2017**, *118*, 372–433.

[11] A. Schneemann, J. L. White, S. Kang, S. Jeong, L. F. Wan, E. S. Cho, T. W. Heo, D. Prendergast, J. J. Urban, B. C. Wood, M. D. Allendorf, V. Stavila, *Chem. Rev.* **2018**, *118*, 10775–10839.

[12] H.-C. Zhou, J. R. Long, O. M. Yaghi, *Chem. Rev.* **2012**, *112*, 673–674.

[13] Y. Cui, Y. Yue, G. Qian, B. Chen, *Chem. Rev.* **2012**, *112*, 1126–1162.

[14] L. E. Kreno, K. Leong, O. K. Farha, M. Allendorf, R. P. V. Duyne, J. T. Hupp, *Chem. Rev.* **2012**, *112*, 1105–1125.

[15] H. Wu, Q. Gong, D. H. Olson, J. Li, *Chem. Rev.* **2012**, *112*, 836–868.

[16] E. Barea, C. Montoro, J. A. Navarro, *Chem. Soc. Rev.* **2014**, *43*, 5419–5430.

[17] A. G. MacDiarmid, *Synth. Met.* **1997**, *84*, 27–34.

[18] M. A. Mansour, W. B. Connick, R. J. Lachicotte, H. J. Gysling, R. Eisenberg, *J. Am. Chem. Soc.* **1998**, *120*, 1329–1330.

[19] J.-P. Zhang, Y.-Y. Lin, W.-X. Zhang, X.-M. Chen, *J. Am. Chem. Soc.* **2005**, *127*, 14162–14163.

[20] V. Finsy, C. E. A. Kirschhock, G. Vedts, M. Maes, L. Alaerts, D. E. De Vos, G. V. Baron, J. F. M. Denayer, *Chem. Eur. J.* **2009**, *15*, 7724–7731.

[21] X.-L. Qi, R.-B. Lin, Q. Chen, J.-B. Lin, J.-P. Zhang, X.-M. Chen, *Chem. Sci.* **2011**, *2*, 2214–2218.

[22] Y. Takashima, V. M. Martínez, S. Furukawa, M. Kondo, S. Shimomura, H. Uehara, M. Nakahama, K. Sugimoto, S. Kitagawa, *Nat. Commun.* **2011**, *2*, 168.

[23] H. Ikeda, T. Yoshimura, A. Ito, E. Sakuda, N. Kitamura, T. Takayama, T. Sekine, A. Shinohara, *Inorg. Chem.* **2012**, *51*, 12065–12074.

[24] B. Liu, M. Tu, R. A. Fischer, *Angew. Chem. Int. Ed.* **2013**, *52*, 3402–3405; *Angew. Chem.* **2013**, *125*, 3486 –3489.

[25] J.-H. Wang, M. Li, D. Li, *Chem. Sci.* **2013**, *4*, 1793–1801.

[26] Y. Sakata, S. Furukawa, M. Kondo, K. Hirai, N. Horike, Y. Takashima, H. Uehara, N. Louvain, M. Meilikhov, T. Tsuruoka, S. Isoda, W. Kosaka, O. Sakata, S. Kitagawa, *Science* **2013**, *339*, 193–196.

[27] M. Dong, M. Zhao, S. Ou, C. Zou, C. Wu, *Angew. Chem. Int. Ed.* **2014**, *53*, 1575–1579; *Angew. Chem.* **2014**, *126*, 1601–1605.

[28] Y. Mao, J. Li, W. Cao, Y. Ying, P. Hu, Y. Liu, L. Sun, H. Wang, C. Jin, X. Peng, *Nat. Commun.* **2014**, *5*, 5532.

[29] R. Haldar, R. Matsuda, S. Kitagawa, S. J. George, T. K. Maji, *Angew. Chem. Int. Ed.* **2014**, *53*, 11772–11777; *Angew. Chem.* **2014**, *126*, 11966–11971.

[30] J. S. Ovens, D. B. Leznoff, *Chem. Mater.* **2015**, *27*, 1465–1478.

[31] Y. Wang, Q. Yang, M. Zhao, J. Wu, B. Su, *Anal. Chem.* **2018**, *90*, 10780–10785.

[32] S. Yuan, L. Feng, K. Wang, J. Pang, M. Bosch, C. Lollar, Y. Sun, J. Qin, X. Yang, P. Zhang, Q. Wang, L. Zou, Y. Zhang, L. Zhang, Y. Fang, J. Li, H. Zhou, *Adv. Mater.* **2018**, *30*, 1704303.

[33] M. Ding, X. Cai, H.-L. Jiang, *Chem. Sci.* **2019**, *10*, 10209–10230.

[34] M. Albrecht, M. Lutz, A. L. Spek, G. van Koten, *Nature* **2000**, *406*, 970–974.

[35] S. Supriya, S. K. Das, *J. Am. Chem. Soc.* **2007**, *129*, 3464–3465.

[36] Z. Huang, P. S. White, M. Brookhart, *Nature* **2010**, *465*, 598–601.

[37] S. H. Lim, M. M. Olmstead, A. L. Balch, *J. Am. Chem. Soc.* **2011**, *133*, 10229–10238.

[38] S. H. Lim, M. M. Olmstead, A. L. Balch, *Chem. Sci.* **2012**, *4*, 311–318.

[39] J. S. Costa, S. Rodríguez-Jiménez, G. A. Craig, B. Barth, C. M. Beavers, S. J. Teat, G. Aromí, *J. Am. Chem. Soc.* **2014**, *136*, 3869–3874.

[40] P. Galer, R. C. Korošec, M. Vidmar, B. Šket, *J. Am. Chem. Soc.* **2014**, *136*, 7383–7394.

[41] G. Zhang, J. Lu, M. Sabat, C. L. Fraser, *J. Am. Chem. Soc.* **2010**, *132*, 2160–2162.

[42] G. R. Krishna, M. S. R. N. Kiran, C. L. Fraser, U. Ramamurty, C. M. Reddy, *Adv. Funct. Mater.* **2013**, *23*, 1422–1430.

[43] H. Imoto, S. Tanaka, T. Kato, T. Yumura, S. Watase, K. Matsukawa, K. Naka, *Organometallics* **2016**, *35*, 3647–3650.

[44] S. Ito, A. Hirose, M. Yamaguchi, K. Tanaka, Y. Chujo, *J. Mater. Chem. C* **2016**, *4*, 5564–5571.

[45] C. Goze, G. Ulrich, L. J. Mallon, B. D. Allen, A. Harriman, R. Ziessel, *J. Am. Chem. Soc.* **2006**, *128*, 10231–10239.

[46] M. Yamaguchi, S. Ito, A. Hirose, K. Tanaka, Y. Chujo, *J. Mater. Chem. C* **2016**, *4*, 5314–5319.

[47] R. Yoshii, K. Suenaga, K. Tanaka, Y. Chujo, *Chem. Eur. J.* **2015**, *21*, 7231–7237.

[48] K. Suenaga, K. Tanaka, Y. Chujo, *Chem. Eur. J.* **2017**, *23*, 1409–1414.

[49] P. Chen, H. Zhang, L. Niu, Y. Zhang, Y. Chen, H. Fu, Q. Yang, Adv. Funct. Mater. **2017**, *27*, 1700332.

[50] J.-Y. Zhu, C.-X. Li, P.-Z. Chen, Z. Ma, B. Zou, L.-Y. Niu, G. Cui, Q.-Z. Yang, *Mater. Chem. Front.* **2020**, *4*, 176–181.

[51] S. Ohtani, M. Gon, K. Tanaka, Y. Chujo, *Chem. Eur. J.* **2017**, *23*, 11827–11833.

[52] K. Suenaga, K. Uemura, K. Tanaka, Y. Chujo, *Polym. Chem.* **2020**, *11*, 1127–1133.

[53] F. P. Macedo, C. Gwengo, S. V. Lindeman, M. D. Smith, J. R. Gardinier, *Eur. J. Inorg. Chem.* **2008**, *2008*, 3200–3211.

[54] R. Yoshii, A. Hirose, K. Tanaka, Y. Chujo, *Chem. Eur. J.* **2014**, *20*, 8320–8324.

[55] R. Yoshii, A. Hirose, K. Tanaka, Y. Chujo, *J. Am. Chem. Soc.* **2014**, *136*, 18131–18139.

[56] S. Ito, K. Tanaka, Y. Chujo, *Inorganics* **2019**, *7*, 100.

[57] L. Bourget-Merle, M. F. Lappert, J. R. Severn, *Chem. Rev.* **2002**, *102*, 3031–3066.

[58] W. E. Piers, D. J. H. Emslie, *Coordin Chem. Rev.* **2002**, *233*, 131–155.

[59] Y.-C. Tsai, *Coordin Chem. Rev.* **2012**, *256*, 722–758.

[60] C. Camp, J. Arnold, *Dalton Trans.* **2016**, *45*, 14462–14498.

[61] Y. Suzuki, T. Kato, H. Huang, I. Yoshikawa, T. Mutai, H. Houjou, *J. Photochem. Photobio. Chem.* **2019**, *385*, 112096.

[62] M. J. Frisch, G. W. Trucks, H. B. Schlegel, G. E. Scuseria, M. A. Robb, J. R. Cheeseman, G. Scalmani, V. Barone, G. A. Petersson, H. Nakatsuji, X. Li, M. Caricato, A. V. Marenich, J. Bloino, B. G. Janesko, R. Gomperts, B. Mennucci, H. P. Hratchian, J. V. Ortiz, A. F. Izmaylov, J. L. Sonnenberg, D. Williams-Young, F. Ding, F. Lipparini, F. Egidi, J. Goings, B. Peng, A. Petrone, T. Henderson, D. Ranasinghe, V. G. Zakrzewski, J. Gao, N. Rega, G. Zheng, W. Liang, M. Hada, M. Ehara, K. Toyota, R. Fukuda, J. Hasegawa, M. Ishida, T. Nakajima, Y. Honda, O. Kitao, H. Nakai, T. Vreven, K. Throssell, J. A. Montgomery, Jr., J. E. Peralta, F. Ogliaro, M. J. Bearpark, J. J. Heyd, E. N. Brothers, K. N. Kudin, V. N. Staroverov, T. A. Keith, R. Kobayashi, J. Normand, K. Raghavachari, A. P. Rendell, J. C. Burant, S. S. Iyengar, J. Tomasi, M. Cossi, J. M. Millam, M. Klene, C. Adamo, R. Cammi, J. W. Ochterski, R. L. Martin, K. Morokuma, O. Farkas, J. B. Foresman, and D. J. Fox, *Gaussian 16 Rev. C.01*, Wallingford, CT, **2016**.

[63] Y. Zhao, D. G. Truhlar, *Theor. Chem. Acc.* **2008**, *120*, 215–241.

[64] T. Schaefer, G. H. Penner, *Can. J. Chem.* **1988**, *66*, 1635–1640.

[65] T. Schaefer, R. Sebastian, *Can. J. Chem.* **1989**, *67*, 1148–1152.

[66] D. C. Spellmeyer, P. D. J. Grootenhuis, M. D. Miller, L. F. Kuyper, P. A. Kollman, *J. Phys. Chem.* **1990**, *94*, 4483–4491.

[67] F. R. Jensen, D. S. Noyce, C. H. Sederholm, A. J. Berlin, *J. Am. Chem. Soc.* **1960**, *82*, 1256–1257.

[68] R. K. Harris, N. Sheppard, *Proc. Chem. Soc.* **1961**, 418–419.

[69] A. Loewenstein, T. M. Connor, *Ber. Bunsenges. Phys. Chem.* **1963**, *67*, 280–295.

[70] L. L. Anderson, J. Arnold, R. G. Bergman, *Org. Lett.* **2004**, *6*, 2519–2522.

[71] S. Varghese, S. Das, *J. Phys. Chem. Lett.* **2011**, *2*, 863–873.

[72] N. J. Hestand, F. C. Spano, *Chem. Rev.* **2018**, *118*, 7069–7163.

[73] T. Higashi, *ABSCOR. Program for Absorption Correction*, Rigaku Corporation, **1995**.

[74] G. M. Sheldrick, *Acta. Cryst. A* **2015**, *71*, 3–8.

[75] G. M. Sheldrick, *Acta Cryst. C* **2015**, *71*, 3–8.

[76] K. Wakita, *Yadokari-XG. Program for Crystal Structure Analysis*, **2000**.

[77] C. B. Hübschle, G. M. Sheldrick, B. Dittrich, *J. Appl. Cryst.* **2011**, *44*, 1281–1284.

[78] L. J. Farrugia, *J. Appl. Cryst.* **1997**, *30*, 565–565.

[79] A. Boultif, D. Louër, *J. Appl. Cryst.* **2004**, *37*, 724–731.

[80] J. W. Visser, *J. Appl. Cryst.* **1969**, *2*, 89–95.

For Table of Contents only
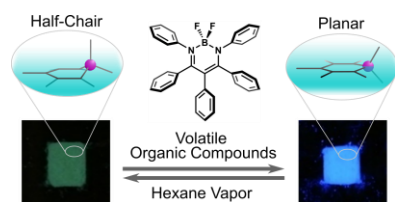
A propeller-shaped boron *β*-diketiminate complex exhibits a reversible color change of fluorescence originating from pseudopolymorphism. The emission color rapidly changes from green to blue when its pure crystals are exposed to an appropriate group of volatile organic compounds and *vice versa*. Such luminescent color changes are derived from crystal–crystal transitions accompanied by the planar-to-half-chair conformational changes of the complex. The small energy differences between the conformers of the complex can afford this pseudopolymorphic behavior.